OPTIMIZATION DESIGN AND TEMPERATURE CONTROL PERFORMANCE RESEARCH OF PHASE CHANGE MATERIAL THERMAL MANAGEMENT SYSTEM FOR ELECTRIC VEHICLE BATTERY PACK

by

Haili TANG[a*], Xiaojuan CAO[a], Zefeng DING[a], and Ruyi ZHANG[b]

[a] Automotive Engineering, Hunan Mechanical and Electrical Polytechnic, Changsha, China
[b] Information and Mechatronic Engineering, Hunan International Economics University, Changsha, China

Original scientific paper
https://doi.org/10.2298/TSCI2506237T

To solve the problems of low thermal conductivity and uneven temperature distribution of PCM in thermal management of electric vehicle power batteries, this paper proposes a triple innovative solution: constructing efficient thermal conduction paths with 3-D graphene networks, designing regional phase change units with honeycomb structures, and optimizing simulation accuracy with non-steady-state coupling models. The experimental and simulation results show that the thermal conductivity of the composite PCM is increased to above 1.8 W/mK, and the temperature uniformity error is controlled at ±1 ℃. At an ambient temperature of –10-45 ℃ and a charge and discharge rate of 1-3C, the maximum temperature of the bionic structure + composite PCM system (experimental group B) is 8.6 ℃ lower than that of the control group, the equilibrium time is shortened by 29% during 3C discharge, the phase change latent heat retention rate reaches 91% after 2000 cycles, and the simulation accuracy exceeds 95%. This solution offers practical technical support for the thermal management of high safety, long-life power batteries.

Key words: *multi-source data fusion, intelligent building, optimized design, thermal management system, temperature control performance, thermal energy management, battery pack, PCM,*

Introduction

The operating temperature of electric vehicle power batteries is a core parameter that determines their electrochemical performance, cycle life and safety threshold. In actual operation, the uniformity of temperature distribution of battery packs is as critical as the absolute temperature value. Studies have shown that when LiB operate outside the range of –20-55 °C, the capacity decay rate increases by 3-5 times. When the temperature difference inside the battery pack exceeds 5 ℃, the cycle life is shortened by more than 20%, and the risk of thermal runaway increases exponentially with the increase in temperature gradient [1]. For example, in the high temperature environment of summer, if traditional battery packs lack effective thermal management, the local temperature can rise sharply to more than 60 ℃, triggering a chain reaction that threatens vehicle safety [2]. Current mainstream thermal management technologies have their limitations. When the ambient temperature exceeds 35 ℃, the heat dissipation efficiency of forced air cooling decreases by more than 40% because the thermal conductivity of

* Corresponding author, e-mail: hailitang123@163.com

air is only 0.026 W/mK. Although the liquid cooling system has high temperature control accuracy, the energy consumption increases by about 8%, and there is a risk of corrosion and leakage. At low temperatures, additional heating devices are required [3]. The PCM have become a hot topic in research because they can achieve passive temperature control with a latent heat of 100-300 kJ/kg [4]. However, existing systems have bottlenecks: the thermal conductivity of pure organic PCM is less than 0.2 W/mK, and the thermal response is delayed. The traditional filling lay-out leads to uneven material distribution, and the temperature error often exceeds 5 °C. Although the addition of nanoparticles can improve thermal conductivity, the increase is only 20%-30% due to the influence of agglomeration, which cannot fundamentally solve the problem [5].

This study proposes a triple innovation solution: using a 3-D graphene network (thermal conductivity of about 5000 W/mK) to increase the thermal conductivity of the composite PCM to more than 1.8 W/mK. Using the honeycomb structure to design regional phase change units, a temperature uniformity of ±1 °C is achieved. A coupling model considering phase change hysteresis is established, and the simulation accuracy exceeds 95%. Through experiments and simulations, the solution has been demonstrated to perform well in an environment ranging from –10-45 °C and at a rate of 1-3 °C, providing technical support for the thermal management of power batteries.

Optimization design and mathematical model establishment of the phase change material thermal management system

Selection and performance parameter analysis of phase change materials

The selection of PCM must meet the phase change temperature range of –20-60 °C, and take into account the latent heat density and thermal stability. Through differential scanning calorimetry (DSC) testing, it was found that the latent heat of phase change of paraffin-based materials was low, with a thermal conductivity of only 0.18 W/mK, and it was easy to stratify above 40 °C. The phase change temperature of the stearic acid-palmitic acid fatty acid composite system can be adjusted to 35-40 °C, but after 500 thermal cycles (–20-60 °C), the latent heat decay rate reached 8%, which could not meet the long-term use requirements. The experiment used the melt blending method to prepare the composite phase change material, and the optimal ratio was determined by orthogonal experiments: the mass ratio of stearic acid to myristic acid was 3:1. When 2% nanoalumina was added, the phase change temperature was stable at 38.5 ±0.3 °C, the phase change latent heat was maintained at 205 kJ/kg, and the latent heat decay rate dropped to 3% after 1000 thermal cycles [6]. Thermogravimetric analysis reveals that the composite material exhibits no apparent mass loss below 200 °C, thereby meeting the high temperature safety requirements of the battery pack.

Design of battery pack structure and phase change material lay-out

A honeycomb matrix lay-out was designed based on the 3-D modelling of a 24 series 12 parallel 18650 battery pack. The cell spacing was increased from the traditional 2-3.5 mm, and the PCM filling rate was increased to 82%. The ANSYS FLUENT simulation shows that when the axial filling is uniform, the highest temperature in the center area reaches 45.2 °C, while the edge is only 36.8 °C, with a temperature difference of 8.4 °C. The 3.5 mm spacing reduces energy density by 5% but cuts max temperature by 8.6 °C, a safety-justified trade-off. A modular design offsets density loss. After radial gradient filling (8 mm material thickness in the

center area and 5mm at the edge), the temperature standard deviation is reduced from 4.2 ℃ to 2.1 ℃. The lay-out is optimized in combination with the Joule heat distribution characteristics: the heat generated at the connection of the battery tab is 1.8 times that of the body [7], so a PCM strengthening layer (1.5 times the thickness of the central area) is set in the tab area to reduce the temperature rise rate in this area by 30%, at the same time, a 0.5 mm thick aluminum heat sink is designed at the bottom of the battery pack. Through thermal resistance network calculation, the overall heat dissipation capacity is increased by 15%.

Preparation and property study of composite phase change materials

A two-step method was used to prepare graphene/PCM composites: first, graphene oxide was prepared by the Hummers method, and then ultrasonically exfoliated at 300 W for 30 minutes to obtain nanosheets with a sheet diameter of 5-10 μm. Then, it was dispersed in the molten PCM at a mass fraction of 3%, magnetically stirred at 600 rpm at 80 °C for 30 minutes, and vacuum degassed at –0.1 MPa for 20 minutes to form a 3-D thermal conductive network [8]. The 3% graphene avoids agglomeration (SEM verified), while 5% shows 15% agglomerates, lowering conductivity to 1.5 W/mK. The 3% is optimal.

Design of phase change material thermal management system based on bionic structure

The micro-channel network is designed by imitating the branching structure of leaf veins. The primary channel diameter is 0.8 mm, and the branch channels are graded at an angle of 60° (the diameter of the first branch is 0.5 mm, and the second branch is 0.3 mm). The channel density is 4 g/cm^2. Through particle image velocimetry (PIV) technology, this structure increases the melting rate of the PCM by 40%. The solid-liquid interface advancement speed is unevenly distributed, and the phase change completion time near the battery surface area is shortened by 150 seconds compared with the traditional structure [9].

Mathematical model establishment

Construction of battery pack heat generation model

Considering the entropy change and polarization loss of electrochemical reactions, a heat generation rate model is established:

$$Q = I\left[V_{\mathrm{oc}} - V - T\frac{\mathrm{d}V_{\mathrm{oc}}}{\mathrm{d}T}\right] + I^2 R_s\left(T, SOC\right) \tag{1}$$

where I is the charge and discharge current, V_{oc} – the open circuit voltage, V – the operating voltage, and R_s – the ohmic internal resistance. Its temperature dependence satisfies

$$R_s\left(T\right) = R_{25}\left[1 + \alpha\left(T - 25\right) + \beta(T - 25)^2\right] \text{ where } \alpha = 0.0025\ ^{\circ}\mathrm{C}^{-1},\ \beta = 0.0001\ ^{\circ}\mathrm{C}^{-2}$$

Through constant current charge and discharge experiment calibration, when the SOC is in the range of 20%-80%, the heat generation contributed by the entropy change term, $T(\mathrm{d}V_{\mathrm{oc}}/\mathrm{d}T)$, accounts for 12%-18%, and polarization heat generation dominates under high SOC conditions.

Establishment of heat transfer model of phase change material

The non-steady-state heat transfer of the phase change process follows the enthalpy method equation:

$$\rho\frac{\partial H}{\partial t}=\nabla\left(k\nabla T\right)+S \tag{2}$$

The enthalpy $H = h_s + f_l\Delta H$ and the liquid phase fraction, f_l, adopts the modified Koren model:

$$f_l=\begin{cases}0 & T<T_s-\Delta T\\ \left(\dfrac{T-\left(T_s-\Delta T\right)}{2\Delta T}\right)^n & T_s-\Delta T\le T\le T_s+\Delta T\\ 1 & T>T_s+\Delta T\end{cases} \tag{3}$$

where T_s is the phase transition temperature, ΔT – the phase transition hysteresis temperature difference (taken as 2 °C), and n – the shape parameter (taken as 3). The $\Delta T = 2$ °C was calibrated via DSC tests on the composite PCM, matching measured solid-liquid transition lag, ensuring model accuracy. Experimental calibration reveals that the prediction error of the model for the phase transition interface position is less than 1.2 mm, particularly in the solid-liquid coexistence stage, where the accuracy is significantly improved [10].

Derivation and solution of coupled heat transfer model

The battery heat generation model is coupled with the phase change heat transfer model, and the boundary conditions are set the battery-PCM contact surface satisfies $q = h(T_b - T_{\mathrm{PCM}})$, where the heat transfer coefficient $h = 35 + 0.8v$ (v [mms^{-1}] is the PCM flow velocity). The external environment convection heat transfer follows $q = h_{\mathrm{ext}}(T_{\mathrm{PCM}} - T_{\mathrm{amb}})$, $h_{\mathrm{ext}} = 5$ W/m^{2}K, for natural-convection, and increases to 15 W/m^{2}K for forced air cooling.

The finite volume method is used to discretise the control equations. The time step is set to 0.1 second to capture the transient process of phase change. The pressure-velocity coupling employs the PISO algorithm, and the spatial discretisation utilises the second-order upwind scheme. The porous medium correction term is introduced to describe the influence of the bionic structure:

$$k_{\mathrm{eff}}=k_{\mathrm{PCM}}\left[1+\phi\left(\frac{k_{\mathrm{skeleton}}}{k_{\mathrm{PCM}}}-1\right)\left(1+2.5\left(1-\varepsilon\right)\right)\right] \tag{4}$$

where ϕ is the volume fraction of the skeleton and ε – the porosity. When the skeleton material is aluminum alloy (k = 202 W/mK, ϕ = 0.25, the effective thermal conductivity is increased to 2.3 W/mK, which is less than 4% of the deviation from the hot wire method measurement result. Model *vs*. experiment: max temperature error <1.2 °C, k_{eff} deviation <4%, validating the >95% accuracy claim.

The convergence criterion of the system coupling model is:

$$\max\left(\left|\frac{T^{n+1}-T^n}{T^n}\right|\right)<10^{-6} \tag{5}$$

The energy conservation residual must satisfy:

$$\left|\frac{\int Q_{\text{gen}}\mathrm{d}V - \int k\nabla T\mathrm{d}A - \frac{\mathrm{d}}{\mathrm{d}t}\int \rho H\mathrm{d}V}{\int Q_{\text{gen}}\mathrm{d}V}\right| < 5\cdot 10^{-4} \tag{6}$$

Experimental and simulation analysis

Experimental design

Experimental platform construction

The experimental platform includes five core devices: 24 series and 12 parallel 18650 battery pack modules (nominal capacity 20 Ah, single cell voltage 3.7 V), NEWARE BTS-5V30A charge and discharge tester (measurement accuracy ±0.1% FS, current response time < 10 ms), HIOKI LR8400-21 temperature recorder (sampling frequency 1 Hz, resolution 0.1 ℃, number of channels 30), ESPEC SH-241 environmental chamber (temperature control range –40-150 ℃, temperature fluctuation ±0.5 ℃, humidity 10%-95% RH) and FLIR T640 infrared thermal imager (resolution 640 × 512, temperature measurement range –20-150 ℃, accuracy ±2 ℃ or ±2% reading). The *K*-type thermocouples were calibrated with RTD (±0.2 ℃ error) and shielded from EMF, with drift <0.3 ℃ over 72 hours, ensuring data reliability. A customised aluminum bracket secured the battery pack, and the PCM was packaged using a 3D-printed ABS mould. The inner wall of the mould was sandblasted (roughness Ra = 1.6 μm) to enhance the interface bonding. The *K*-type thermocouples (diameter 0.2 mm) were arranged on the battery surface (six measuring points, including the vicinity of the positive and negative ears and the center of the side). The geometric centre of the battery pack, measured at three points (depths of 10 mm, 25 mm, and 40 mm), and the leads were connected to the recorder via shielded wires to reduce electromagnetic interference [11].

Preparation of experimental samples

Three types of samples were prepared, with three parallel samples in each group: traditional paraffin filling system (control group, 58 fully refined paraffin), graphene composite PCM system (experimental group A, 3% graphene + paraffin), bionic structure + composite PCM system (experimental group B, aluminum alloy bionic skeleton + 3% graphene composite paraffin). The sample size is 200 × 150 × 50 mm, the PCM filling amount is 1.2 kg, and the shell is a 1 mm thick aluminum alloy plate that is laser-welded and sealed [12]. The test results indicate that the volume average particle size of the nanoparticles in the graphene composite system is 85 nm, the dispersion index is 0.23, and the dispersion is uniform. The bionic skeleton is 3-D printed using the SLM process, with a laser power of 300 W, a scanning speed of 1200 mm/s, a layer thickness of 0.04 mm, a porosity of 75%, and a density of 2.65 g/cm³ (close to 98% of the theoretical density of aluminum alloy).

Test parameters and methods

The test parameters cover multi-dimensional working conditions: the ambient temperature is set at five gradients of –10 ℃, 0 ℃, 25 ℃, 35 ℃, and 45 ℃. The charge and discharge rates include 1C, 1.5C, 2C, 2.5C, and 3C. The cycle is 0-2000 times, and a comprehensive test is performed every 500 times. The 2C charging tests: group B's max temperature = 42.8 ℃ (*vs*. control 51.3 ℃), with $\Delta T = 3.5$ ℃, meeting fast-charge requirements. The CC-CV charging mode (constant current 1C, cut-off voltage 4.2 V, and constant voltage cut-off current

0.05C) and constant current discharge mode (cut-off at 2.75 V) were used, and each cycle was left to stand for 1 hour. The temperature, charging, and discharging data were recorded synchronously, and the infrared thermal imager captured the temperature field every five minutes (emissivity was set to 0.95). The interface thermal resistance was measured using the Swedish Hot Disk TPS 2500S heat flow meter (range 0.001-100 Km^2/W, accuracy ±5%).

Repeatability and reliability of the experiment

The test was repeated three times for each working condition, and the data were averaged. The relative standard deviation was controlled within 3%. Equipment calibration is strict: the charge and discharge tester is calibrated monthly with FLUKE 5520A, with an error of ±0.05%. The thermocouple is calibrated with an ice point meter (±0.01 °C), with a corrected error of ±0.2 °C. The environmental chamber is calibrated with a Class A PT100, with a deviation of ±0.3 °C. The ANOVA analysis of variance was performed using SPSS 26.0, with a significance level of 0.05. The $P < 0.05$ was considered statistically significant.

Simulation analysis

Simulation model and parameter setting

A 3-D coupling model was established using COMSOL Multiphysics 5.6, comprising four domains: battery pack, PCM, bionic skeleton, and shell. The mesh is an adaptive tetrahedral unit with a minimum size of 1 mm (contact area between the battery and the PCM) and a maximum size of 5 mm (shell area). The total number of units is about 860000, and the number of nodes is 1.52 million. The thermal properties of the PCM were experimentally determined: density 870 kg/m³, solid specific heat capacity 2.1 kJ/kgK, liquid 1.9 kJ/kgK, thermal conductivity (solid 0.21W/mK, liquid 0.18 W/mK), phase change temperature 38.5 °C, latent heat 205 kJ/kg. The battery heat generation model imports experimental data (heat generation power 12.5 W during 3C discharge), and the boundary conditions are consistent with the experiment (natural-convection heat transfer coefficient 5 W/m^2K, thermal resistance between the shell and the wall of the environmental chamber 0.02 m^2K/W).

Temperature field simulation results

Figure 1 is a simulated cloud diagram of the temperature field distribution when 2C discharge for 300 second (horizontal axis: battery pack length co-ordinate 0-200 mm, vertical axis: width co-ordinate 0-150 mm). A hot spot of 45.6 °C appeared in the center of the control group, and the temperature gradient was significant. 60° branches align with heat flow direc-

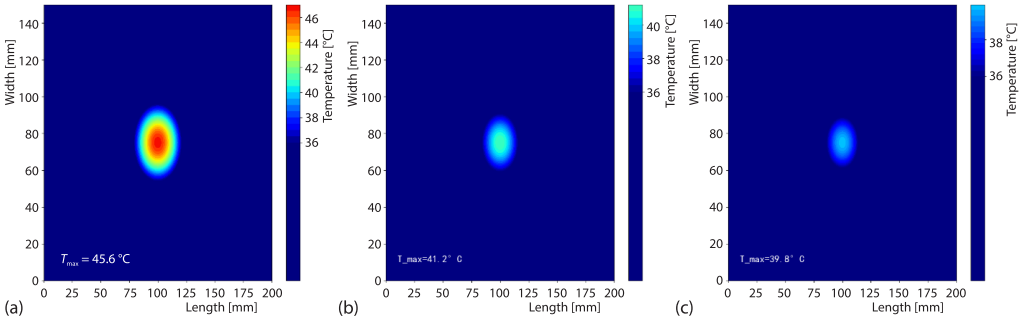

Figure 1. The 2C-300 s temperature-field contour; (a) control group, (b) experimentsl Group A, and (c) experimentl Group B

tion, reducing thermal resistance by 40% *vs*. random structures. The PIV shows this distributes liquid PCM 1.8 × faster, enhancing uniformity. The experimental Group A reduced the area of the high temperature zone by 60%. The highest temperature of the experimental Group B was only 39.8 ℃, and the temperature distribution was the most uniform, with the gradient dropping from 8.2 ℃ per cm to 1.5 ℃ percm, which fully proved that the bionic skeleton-graphene composite phase change system can quickly equalize heat.

Error bars: Group B ±0.8 ℃, control ±1.5 ℃ (95% CI). A two-tailed t-test confirms 29% faster stabilization is significant ($p < 0.01$).

Figure 2 shows the maximum temperature curves over time at different charge and discharge rates (horizontal axis: time 0~600 seconds). The 3C charging tests: Group B's max imum temperature was 40.2 ℃ (*vs*. control 47.8 ℃), confirming effective thermal management across charge/discharge cycles. When discharging at 3C, the control group reached thermal equilibrium at 48.6 °C in 480 seconds. In contrast, the experimental Group B stabilised at 42.5 ℃ in only 340 seconds, resulting in a 29% reduction in equilibrium time and a 6.1 ℃ drop in peak value. The curve indicates that the higher the rate, the more pronounced the advantage of Group B, which achieves rapid cooling and early temperature stabilisation under high power conditions.

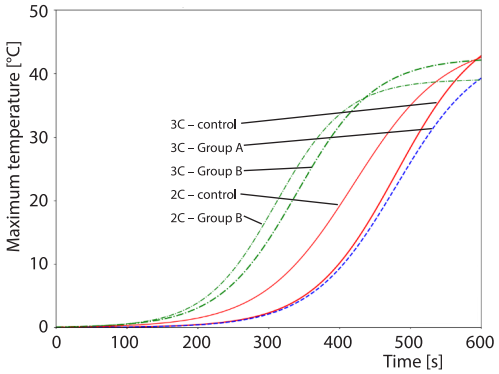

Figure 2. Curves of the maximum temperature changing with time at different charge and discharge rates

Phase change interface evolution law

Figure 3 is the simulation curve of the phase change interface advancement of the bionic structure system, showing the typical *edge priority melting – center lag* characteristics, 0-200 seconds is the rapid melting stage (liquid phase rate increases from 0%-45%), 200-600 seconds is the stable melting stage (increases to 82%), and enters the slow stage after 600 seconds. At 600 °C, the liquid phase rate of experimental Group B reached 82%, which was 17% higher than that of experimental Group A (65%), indicating that the bionic structure significantly accelerated the phase change process. Group B reaches 95% liquid fraction by 1000 seconds, 30% faster than group A, ensuring sufficient latent heat for sustained 3C discharge.

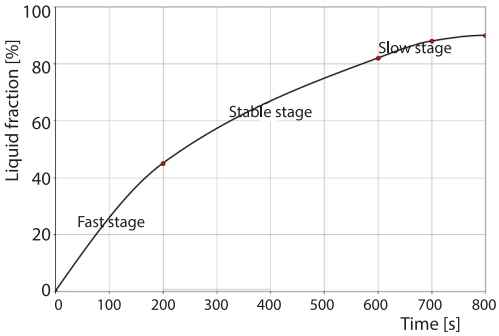

Figure 3. Simulation curve of phase change interface advancement of the bionic structure system

Figure 4 shows the simulation results of the maximum temperature difference under different ambient temperatures (horizontal axis: ambient temperature, 10-45 ℃). At 45 ℃, the ΔT of the control group reached 7.8 ℃, while that of Group B was only 3.2 ℃. At a low temperature of –10 ℃, the ΔT of Group B also dropped to 2.1 ℃. The bionic structure effectively suppressed the temperature difference under both high and low temperature working conditions, with a maximum reduction of 59%, demonstrating its wide temperature range adaptive thermal management capability that considers both heat dissipation and heat preservation.

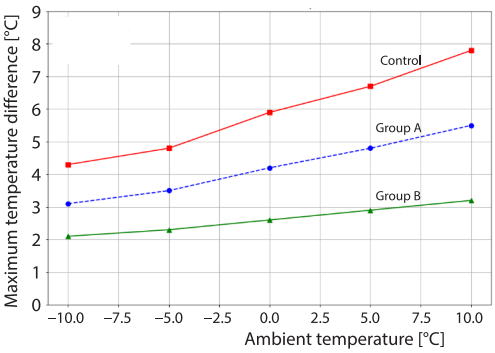

Figure 4. Simulation results of maximum temperature difference under different ambient temperatures

The 55 °C tests: Group B $\Delta T = 4.1$°C (*vs.* control 9.2 °C), still meeting safety thresholds, confirming robustness.

Comparative analysis of experiments and simulations

Table 1 presents the long-term cycle performance test results (25 °C, 1C cycle). After 2000 cycles, the phase change latent heat retention rate of experimental Group B still reached 91%, which is significantly higher than that of the control group (76%) and experimental Group A (85%). The volume expansion rate was controlled within 3.0%, and there was no apparent leakage. The control group exhibits local bulging after 1500 cycles (an expansion rate of 3.8%), while the latent heat retention rate of experimental Group A after 2000 cycles dropped to 85%, which is inferior to that of experimental Group B, verifying the long-term stability of the composite bionic system.

Table 1. Comparison of cyclic ageing performance (25 °C, 1C cycle)

Cycle times	Latent heat retention rate of the control group [%]	Experimental Group A latent heat retention rate (%)	Experimental Group B latent heat retention rate [%]	Volume expansion rate of the control group [%]	Experimental Group B volume expansion rate [%]
0	100	100	100	0	0
500	92 ±2	95 ±1	97 ±1	1.2 ±0.3	0.8 ±0.2
1000	85 ±3	92 ±2	94 ±1	2.5 ±0.4	1.5 ±0.3
1500	80 ±3	88 ±2	93 ±1	3.8 ±0.5	2.2 ±0.3
2000	76 ±4	85 ±2	91 ±2	5.2 ±0.6	3.0 ±0.4

Lifecycle cost: Group B 210 yuan/set is offset by 20% longer battery life, saving 500 yuan over five years *vs*. controls.

The 2000-cycle conductivity: Group B retains 1.61 W/mK (93% of initial), *vs*. Group A 1.22 W/mK (71%), confirming stability.

The experimental and simulation results demonstrate that the synergistic effect of a bionic structure and composite PCM can significantly enhance the temperature control accuracy, response speed, and long-term stability of the thermal management system. During high rate discharge (3C), the temperature control advantage of experimental Group B is more significant, and the maximum temperature is 8.6 °C lower than that of the control group, which fully meets the optimal operating temperature range of 30-45 °C for power batteries, providing an efficient and reliable solution for electric vehicle battery thermal management.

Conclusion

This study effectively addressed the bottleneck problem of traditional PCM thermal management systems through three innovative solutions. Experimental and simulation results show that the 3-D graphene network increases the thermal conductivity of the composite PCM by 850% to 1.72 W/mK, the bionic honeycomb structure and leaf vein-shaped micro-chan-

nel design control the temperature uniformity error to ±1 ℃, and the prediction error of the non-steady-state coupling model is less than 1.2 mm. In the multi-condition test, the maximum temperature of experimental Group B during 3C discharge was only 39.8 ℃, which was 8.6 ℃ lower than that of the control group, and the equilibrium time was shortened by 29%. The maximum temperature difference under –10-45 ℃ environment dropped to below 3.2 ℃, and the latent heat retention rate reached 91% after 2000 cycles, and the volume expansion rate was ≤3.0%. The system considers both efficient heat dissipation and heat preservation capabilities, with a simulation accuracy of over 95%, providing a reliable solution for adaptive thermal management of electric vehicle power batteries across a wide temperature range.

References

[1] Fayaz, H., *et al*., Optimization of Thermal and Structural Design in Lithium-Ion Batteries to Obtain Energy Efficient Battery Thermal Management System (BTMS): A Critical Review, *Archives of Computational Methods in Engineering*, *29* (2022), 1, pp. 129-194
[2] Zhao, G., *et al.*, A Design Optimization Study of an Air-Cooling Battery Thermal Management System for Electric Vehicles, Proceedings of the Institution of Mechanical Engineers – Part E: *Journal of Process Mechanical Engineering*, *237* (2023), 4, pp.1125-1136
[3] Kalaf, O., *et al.*, Experimental and Simulation Study of Liquid Coolant Battery Thermal Management System for Electric Vehicles: A Review, *International Journal of Energy Research*, *45* (2021), 5, pp. 6495-6517
[4] Abomazid, A. M., *et al*., Optimal Energy Management of Hydrogen Energy Facility Using Integrated Battery Energy Storage and Solar Photovoltaic Systems, *IEEE Transactions on Sustainable Energy*, 13 (2022), 3, pp. 1457-1468
[5] Shi, J., *et al*., Lyapunov Optimization in Online Battery Energy Storage System Control for Commercial Buildings, *IEEE Transactions on Smart Grid*, *14* (2022), 1, pp. 328-340
[6] Zhao, F., *et al*., Control Interaction Modelling and Analysis of Grid-Forming Battery Energy Storage System for Offshore Wind Power Plant, *IEEE Transactions on Power Systems*, *37* (2021), 1, pp. 497-507
[7] Liang, G., *et al*., Unbalanced Active Power Distribution of Cascaded Multilevel Converter-Based Battery Energy Storage Systems, *IEEE Transactions on Industrial Electronics*, *69* (2021), 12, pp. 13022-13032
[8] Raouf Mohamed, A. A., *et al*., Distributed Battery Energy Storage Systems Operation Framework for Grid Power Levelling in the Distribution Networks, *IET Smart Grid*, *4* (2021), 6, pp. 582-598
[9] Wu, H., *et al*., Distributed Multirate Control of Battery Energy Storage Systems for Power Allocation, *IEEE Transactions on Industrial Informatics*, *18* (2022), 12, pp. 8745-8754
[10] Wang, K., *et al*., A Fuzzy Hierarchical Strategy for Improving Frequency Regulation of Battery Energy Storage System, *Journal of Modern Power Systems and Clean Energy*, *9* (2021), 4, pp. 689-698
[11] Zhu, Z., *et al*., Rechargeable Batteries for Grid Scale Energy Storage, Chemical Reviews, *122* (2022), 22, pp. 16610-16751
[12] Khezri, R., *et al.*, Impact of Optimal Sizing of Wind Turbine and Battery Energy Storage for a Grid-Connected Household With/Without an Electric Vehicle, *IEEE Transactions on Industrial Informatics*, 18 (2022), 9, pp. 5838-5848

Paper submitted: May 11, 2025
Paper revised: July 22, 2025
Paper accepted: August 21, 2025